

TECHNICAL  
REPORTS: METHODS

10.1002/2017GC006946

## Key Points:

- We developed a quantum diamond microscope (QDM) for imaging magnetic fields produced by geological samples
- This instrument offers a combination of superior spatial resolution (5  $\mu\text{m}$ ), magnetic sensitivity (20  $\mu\text{T} \cdot \mu\text{m}/\text{Hz}^{1/2}$ ), and wide field of view (4 mm)
- We demonstrate the application of this instrument to magnetic mapping of several terrestrial and meteoritic rock samples

## Supporting Information:

- Supporting Information S1
- Data Set S1

## Correspondence to:

R. Walsworth,  
rwalsworth@cfa.harvard.edu

## Citation:

Glenn, D. R., R. R. Fu, P. Kehayias, D. Le Sage, E. A. Lima, B. P. Weiss, and R. L. Walsworth (2017), Micrometer-scale magnetic imaging of geological samples using a quantum diamond microscope, *Geochem. Geophys. Geosyst.*, 18, doi:10.1002/2017GC006946.

Received 3 APR 2017

Accepted 10 JUL 2017

Accepted article online 26 JUL 2017

## Micrometer-scale magnetic imaging of geological samples using a quantum diamond microscope

D. R. Glenn<sup>1</sup>, R. R. Fu<sup>2</sup>, P. Kehayias<sup>3</sup> , D. Le Sage<sup>1</sup> , E. A. Lima<sup>2</sup> , B. P. Weiss<sup>2</sup>, and R. L. Walsworth<sup>1,3</sup>

<sup>1</sup>Department of Physics, Harvard University, Cambridge, Massachusetts, USA, <sup>2</sup>Department of Earth, Atmospheric, and Planetary Sciences, Massachusetts Institute of Technology, Cambridge, Massachusetts, USA, <sup>3</sup>Harvard-Smithsonian Center for Astrophysics, Cambridge, Massachusetts, USA

**Abstract** Remanent magnetization in geological samples may record the past intensity and direction of planetary magnetic fields. Traditionally, this magnetization is analyzed through measurements of the net magnetic moment of bulk millimeter to centimeter sized samples. However, geological samples are often mineralogically and texturally heterogeneous at submillimeter scales, with only a fraction of the ferromagnetic grains carrying the remanent magnetization of interest. Therefore, characterizing this magnetization in such cases requires a technique capable of imaging magnetic fields at fine spatial scales and with high sensitivity. To address this challenge, we developed a new instrument, based on nitrogen-vacancy centers in diamond, which enables direct imaging of magnetic fields due to both remanent and induced magnetization, as well as optical imaging, of room-temperature geological samples with spatial resolution approaching the optical diffraction limit. We describe the operating principles of this device, which we call the quantum diamond microscope (QDM), and report its optimized image-area-normalized magnetic field sensitivity (20  $\mu\text{T} \cdot \mu\text{m}/\text{Hz}^{1/2}$ ), spatial resolution (5  $\mu\text{m}$ ), and field of view (4 mm), as well as trade-offs between these parameters. We also perform an absolute magnetic field calibration for the device in different modes of operation, including three-axis (vector) and single-axis (projective) magnetic field imaging. Finally, we use the QDM to obtain magnetic images of several terrestrial and meteoritic rock samples, demonstrating its ability to resolve spatially distinct populations of ferromagnetic carriers.

## 1. Introduction

Reliable characterization of ancient magnetic fields using geological samples requires the survival of ferromagnetic phases that were present to record the magnetic field of interest. However, metamorphism, aqueous alteration, and surface weathering are common processes that may destroy and replace all or a subset of a rock sample's ferromagnetic minerals. At the same time, erosion may lead to the physical disintegration of rocks and the reassembly of their constituent parts in clastic sediments. As a result of these secondary chemical and physical processes, diachronous populations of ferromagnetic minerals are frequently juxtaposed at the micrometer to millimeter scales. The difficulty of extracting useful paleomagnetic information from such complex samples is a key limiting factor to our understanding of the early Earth magnetic field [e.g., Weiss *et al.*, 2015], the past configuration of lithospheric plates [e.g., Kent *et al.*, 1987], and the stability of the Earth's rotation and geomagnetic field axis in the mantle reference frame [e.g., Swanson-Hysell *et al.*, 2012]. Furthermore, even in the absence of secondary remagnetization, geological samples often contain different populations of ferromagnetic minerals with disparate capacities for recording a high-fidelity, interpretable remanence [Fu *et al.*, 2014a].

Obtaining useful paleomagnetic data from samples with complex geological histories and/or fine-scale mixtures of ferromagnetic grains with varying recording properties requires the isolation of magnetic signal carried by high-fidelity ferromagnetic grains that were magnetized during the time period of interest. Standard paleomagnetic techniques, limited in part by the magnetometer sensitivity, typically measure the net magnetic moment of whole-rock samples with volumes of several cubic centimeters. For such samples, magnetic cleaning techniques such as thermal and alternating-field demagnetization have been used to isolate the magnetization carried by subpopulations of ferromagnetic grains [Tauxe, 2010]. However, magnetic cleaning often does not fully isolate a single population of grains due to overlapping ranges of unblocking

temperatures or coercivities. Furthermore, because the microscopic contexts of ferromagnetic grain populations are generally not directly constrained by magnetic cleaning, correctly identifying the relative age and origin of the magnetization component of interest is often ambiguous.

The development of mapping magnetometers capable of resolving ferromagnetic carriers at the submillimeter scale—such as the SQUID microscope [Weiss *et al.*, 2007; Kawai *et al.*, 2016], magneto-impedance microscopes [Nakamura *et al.*, 2010], magnetoresistance (MR) microscopes [Hankard *et al.*, 2009], magneto-optical imaging (MOI) [Uehara *et al.*, 2010], Hall-effect microscopes [Kletetschka *et al.*, 2013], and the magnetic tunnel junction (MTJ) microscope [Lima *et al.*, 2014]—has led to a new approach for analyzing rock samples with complex, heterogeneous magnetizations. These instruments are capable of imaging the spatial distribution of remanent fields so that they can be spatially correlated with the fine-scale magnetization distribution within a sample [Fu *et al.*, 2014a].

It has recently been demonstrated that nitrogen-vacancy (NV) centers in diamond [Doherty *et al.*, 2013; Schirhagl *et al.*, 2014; Rondin *et al.*, 2014] enable sensitive imaging of static magnetic field distributions with submicrometer spatial resolution [Pham *et al.*, 2011]. Perhaps the simplest and most robust implementation of NV magnetic imaging is the quantum diamond microscope (QDM) [Glenn *et al.*, 2015]. This device consists of a thin (10 nm–10  $\mu\text{m}$ ) layer of NV centers implanted or grown into the surface of a diamond chip that is brought into close proximity with the magnetic sources of interest and interrogated using optically detected magnetic resonance (ODMR) [Gruber *et al.*, 1997]. The QDM is readily applicable to the study of geological samples at room temperature ( $<50^\circ\text{C}$ ) and low ambient magnetic field ( $<50\ \mu\text{T}$ ), making it an attractive platform for spatially resolved measurements of artificial and natural remanent magnetization (NRM). Furthermore, because the NV centers can typically be placed within  $\sim 10\ \mu\text{m}$  of the magnetic sources of interest (or closer, if special care is taken with sample and sensor preparation), even a relatively modest QDM magnetic noise floor of  $\sim 100\ \text{nT RMS}$  is sufficient to detect moments as small as  $\sim 10^{-16}\ \text{A}\cdot\text{m}^2$ , providing sensitivity comparable or superior to scanning SQUID, MR, MOI, Hall-effect, and MTJ microscope technologies. The QDM also allows optical imaging in the same configuration, providing spatially correlated magnetic and optical images of the sample.

## 2. Description of the QDM

### 2.1. Basic Operating Principles

In the QDM implementation described here (Figures 1a and 1b), a diamond sensor chip (labeled as D1–D4 in our experiments; see supporting information Table S1 for details) is placed, NV layer face down, above the polished surface of the rock sample. The sample is mounted on a printed circuit board patterned with a pair of decoupled, crossed stripline microwave resonators. The striplines are excited in-phase (or  $90^\circ$  out-of-phase) to produce a linearly (or circularly) polarized, GHz-frequency magnetic field for driving continuous spin rotations in the NV centers. The NV centers are continuously probed with green laser excitation (wavelength 532 nm, intensity  $10^5$ – $10^7\ \text{W}/\text{m}^2$ ), and their emitted red fluorescence (wavelength 637–800 nm) is imaged with a scientific complementary metal oxide semiconductor (sCMOS) camera.

For geological samples that could be adversely affected by heating during prolonged laser illumination, the diamond chip may be angle-polished such that excitation light is totally internally reflected from the bottom surface and exits the opposite facet (Figure 1b). In contrast, with a square-cut chip and laser light directly impinging on the sample, we observe up to  $\sim 30^\circ\text{C}$  heating above room temperature under realistic imaging conditions for most sample substrates (supporting information Figure S2).

Three pairs of Helmholtz-configured magnet coils produce a spatially homogeneous static field ( $B_0$ ) at the rock sample and NV layer, which can be used to cancel the local Earth's field and provide the NV centers with a controlled magnetic bias. The accuracy of the field nulling achieved with the present system is  $\sim 0.1\ \mu\text{T}$ , comparable to the magnetic sensitivity of our measurements, but could be improved with the use of high-precision current supplies and/or secondary shim coils if needed.

The ODMR measurement proceeds by simultaneous application of optical and microwave fields (the latter denoted  $B_1$ ) to the ensemble of NV centers, generating a spatially dependent NV fluorescence signal with features dependent on the sample-induced, local magnetic field (See supporting information Figure S3 for background on the physics and level structure of NV centers in diamond.) In the absence of microwaves,

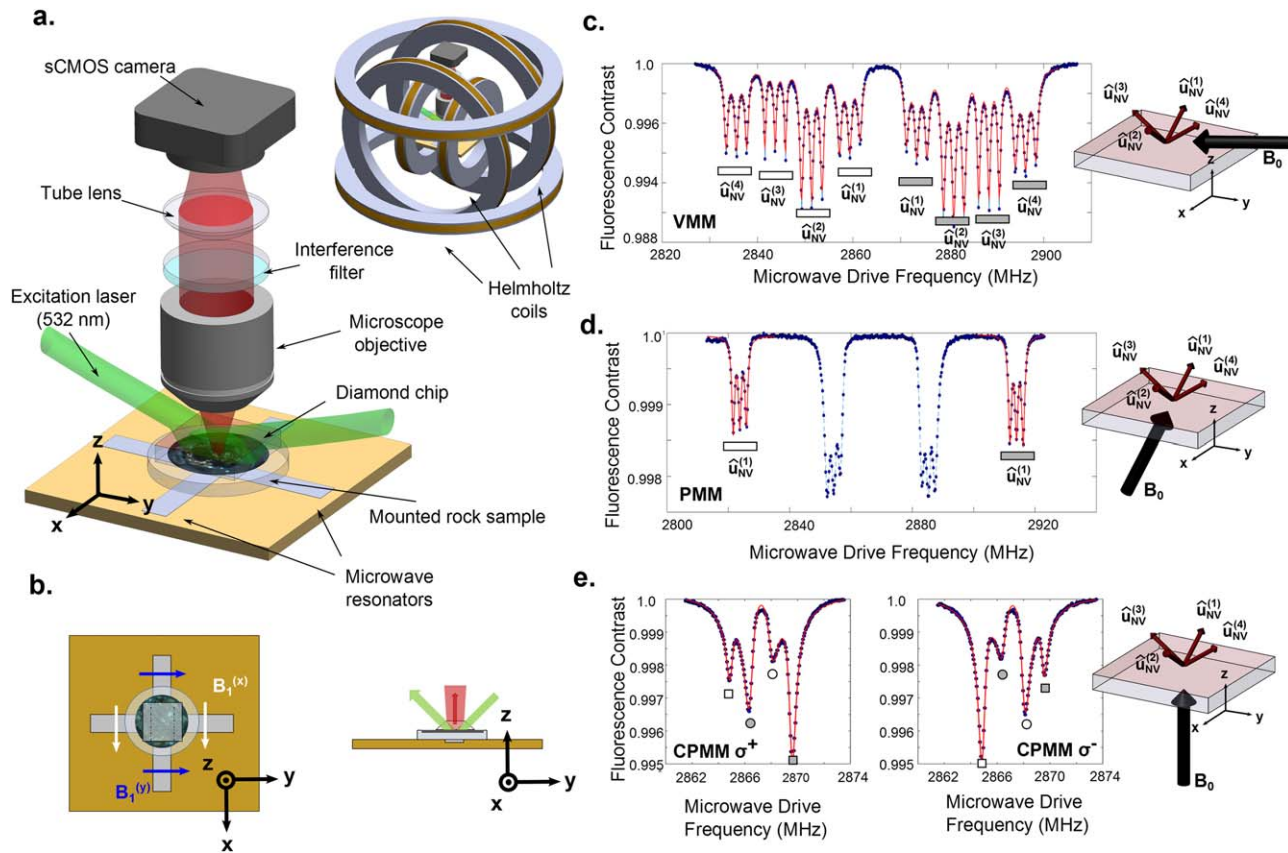


**Figure 1.** Rock magnetic imaging using a quantum diamond microscope (QDM). (a) Schematic of QDM configuration. The rock sample is placed on a glass slide near the focus of a microscope objective. A diamond chip is positioned above it, with a dense layer of nitrogen-vacancy (NV) centers facing down. The NV centers are interrogated using green laser light and continuous microwave driving, with the microwaves delivered by strip-line resonators below the sample mount. Red fluorescence from the NV centers is imaged onto a scientific CMOS camera to map the sample magnetic fields. Inset shows full QDM including three orthogonal pairs of Helmholtz coils that control the bias field  $B_0$  at the NV center layer. (b) Isolated top and side views of the sample mount plus microwave strip-lines, which are driven to produce a resonant field ( $B_1$ ) to manipulate the NV spins. When the strip-lines are driven in phase,  $B_1$  is linearly polarized along  $\hat{x} + \hat{y}$ . When the strip-lines are driven out-of-phase,  $B_1$  is circularly polarized about the  $z$  axis (with polarization vector  $\hat{x} \pm i \hat{y}$ ). Laser light impinges on the NV center layer at the bottom of the diamond chip, and NV fluorescence is imaged through the top of the diamond. (c) Characteristic NV optically detected magnetic resonance (ODMR) spectrum for vector magnetic microscopy (VMM). Inset shows the orientation of  $B_0$ , which projects unequally onto the  $[111]$  diamond lattice directions so that transitions for all four NV orientations are resolved. Each orientation allows two spin transitions,  $\Delta m_s = \pm 1$ , which are further split into triplets due to hyperfine coupling to the  $^{14}\text{N}$  nucleus of the NV center. The  $\Delta m_s = +1$  (or  $\Delta m_s = -1$ ) triplets are indicated with grey (or white) bars. During data acquisition, the  $B_1$  frequency is swept across all resonances, the NV fluorescence is measured at each frequency (blue dots) and a portion of the spectrum is fit (red curve) to determine the local vector magnetic field. (d) ODMR spectrum for projective magnetic microscopy (PMM).  $B_0$  is parallel to one of the  $[111]$  directions, distinguishing it spectrally, while the other three NV orientations are degenerate. The  $B_1$  frequency is scanned and line shapes are fit (red curves) only for the aligned transitions, enabling rapid acquisition of single-axis magnetic field data. In a real experiment, data points corresponding to the nonaligned transitions would not be acquired—they are included here for illustrative purposes only. (e) ODMR spectrum for circularly polarized magnetic microscopy (CPMM). The NV centers are formed from  $^{15}\text{N}$ , resulting in hyperfine doublets instead of the triplets associated with  $^{14}\text{N}$ .  $B_0$  is applied perpendicular to the chip surface, with equal projection on all four  $[111]$  directions, making the four pairs of NV transitions degenerate. Also,  $B_0$  is small, such that the electronic Zeeman shift is weaker than the nuclear hyperfine coupling. Transitions for which the nuclear spin state is  $m_I = +1/2$  (or  $m_I = -1/2$ ) are indicated with squares (or circles). The  $\Delta m_s = +1$  (or  $\Delta m_s = -1$ ) transitions are indicated with grey (or white) markers. In the first (second) plot,  $B_1$  has right- (left-) circular polarization about the  $B_0$  axis, favoring excitation of the  $\Delta m_s = +1$  ( $\Delta m_s = -1$ ) transitions. Data acquisition consists of alternating between circular-polarization orientations while scanning the  $B_1$  frequency and fitting line shapes over the full spectrum (red curve).

the optical excitation induces a baseline fluorescence level by continuously driving the NV population into an excited electronic state, which spontaneously decays (lifetime  $\tau \approx 13$  ns [Robledo *et al.*, 2011]) by emitting red fluorescence. The addition of a microwave  $B_1$  field resonant with one of the ground state spin transitions causes a fraction of the NV population to be transferred from the  $m_s = 0$  to the  $m_s = -1$  or  $m_s = +1$  states. These states, when optically excited, have a finite branching ratio to a long-lived metastable state (lifetime  $\tau \approx 220$  ns [Acosta *et al.*, 2010]), decreasing the emitted fluorescence. Off-resonant microwave driving leaves the baseline fluorescence unchanged. The spin resonance frequency for each NV center is Zeeman-shifted by the local magnetic field, resulting in a spatially varying fluorescence pattern where the light emitted at each position is suppressed below the baseline only if the microwave drive is resonant. In the low-field limit ( $g \mu_B B \ll f_{ZFS}$ , for Landé  $g$ -factor  $g \approx 2$ ,  $\mu_B \approx 14$  GHz/T the Bohr magneton, and  $f_{ZFS} \approx 2.87$  GHz the NV zero-field splitting), the Zeeman shift is  $\Delta f = \pm g \mu_B |B_p|$ , where  $B_p$  is the magnitude of the

local magnetic field projected onto the NV axis. The sign of the shift is positive (negative) for the  $\Delta m_s = +1$  ( $\Delta m_s = -1$ ) spin transition. By sweeping the microwave frequency and collecting a fluorescence image at each increment of microwave frequency, the magnetic field spatial distribution is obtained (supporting information Figure S4). The resulting field map may then be spatially filtered in software to optimize sensitivity at length scales of interest (typically  $\sim 5\text{--}500\ \mu\text{m}$  for the geological samples investigated in this work).

To correlate magnetic field maps with mineralogical properties of the sample, reflected-light microscopy is carried out in-place in the QDM. The green laser excitation beam is turned off and replaced with light from a red light-emitting diode (LED, wavelength  $\sim 660\ \text{nm}$ ). The red light passes through the diamond, reflects off the surface of the sample, and is imaged onto the camera using the same collection optics as for NV fluorescence. In the QDM system we describe here, spherical aberration due to imaging through the diamond chip ( $\sim 500\ \mu\text{m}$  thickness) limits the spatial resolution of reflected-light microscopy to  $\sim 5\ \mu\text{m}$ . This is comparable to the spatial resolution of magnetic imaging in the present QDM system (also limited by spherical aberration, as well as sample roughness, which is of similar magnitude), and sufficient in practice to enable coregistration with high resolution optical images acquired in other instruments. The problem of spherical aberration in the QDM can be overcome by designing thinner diamond chips, or by introducing additional correcting lenses into the detection path.

We note that optical diffraction fundamentally limits spatial resolution, in both magnetic maps and reflected-light microscopy. Using a high numerical aperture (NA) objective lens, the diffraction limit is about  $\sim 0.4\ \mu\text{m}$  for our camera-based QDM implementation [Le Sage *et al.*, 2013]. Diffraction can, in principle, be circumvented by using super-resolution imaging techniques with scanning excitation [Maurer *et al.*, 2010], making the QDM potentially suitable for direct imaging of single ferromagnetic grains in submicrometer thickness sections.

## 2.2. Modes of QDM Operation

### 2.2.1. Vector Magnetic Microscopy (VMM)

The choice of  $B_0$  and  $B_1$  allows the QDM instrument to be operated in several different modes, with associated tradeoffs in sensitivity, ease of calibration, and ambient field cancellation. The most general approach is NV vector magnetic microscopy (VMM), in which the  $B_0$  field is aligned with nonzero, unequal projections onto all four NV orientations (each coinciding with one of the four [111] diamond crystal axes). The magnitude of  $B_0$  is typically set to  $\sim 1\ \text{mT}$  such that all ODMR lines are fully resolved (Figure 1c). The frequency of the linearly polarized  $B_1$  field is swept across the entire range of NV resonances, providing full (three-axis) vector magnetic field information in each pixel of the image. The current applied to the Helmholtz coils is then reversed and the measurement repeated. The sum of these two measured field maps represents the signal from remanent magnetization carried by ferromagnetic grains with coercivity  $> B_0$ . The difference between maps represents the induced magnetization, which may be used to localize paramagnetic, superparamagnetic, and other low-coercivity carriers. We achieve a field reversal precision of  $\sim 10^{-4}$  in the present system, corresponding to a residual bias  $B_0^{(r)} < 0.1\ \mu\text{T}$  in the ferromagnetic (measurement sum) field map. (The residual bias  $B_0^{(r)}$  is defined as the vector sum of the positively and negatively oriented applications of  $B_0$ , and is measured in a region of the field map far from any magnetic sources.) Using the VMM technique, we obtain an image-area-normalized sensitivity of about  $\sim 1\text{--}100\ \mu\text{T}\cdot\mu\text{m}/\text{Hz}^{1/2}$ , depending on details of the NV-diamond sensor and the configuration of fluorescence excitation and collection optics.

### 2.2.2. Projective Magnetic Microscopy (PMM)

In the second ODMR technique, we restrict the set of microwave transition frequencies scanned to enable faster data acquisition. In general, magnetic field sensitivity is improved by reducing microwave scan range, which is feasible if all regions of the sample produce magnetic fields that lie in a restricted region of the Zeeman-shifted ODMR spectrum. For applications that require only single-axis magnetic imaging,  $B_0$  may be aligned parallel to just one of the [111] diamond lattice directions, such that the spin transition frequencies for the NV orientation along that orientation are maximally split. Transition frequencies for the other three orientations are degenerate due to tetrahedral symmetry of the lattice.

The ODMR frequency  $f$  is swept only over the selected pair of resonances, and ideally over only over the part of each resonance with maximum slope,  $dS/df$ , for  $S$  the ODMR fluorescence signal contrast. This can result in particularly efficient sensing due to the reduced signal acquisition time per sweep, and the strong dependence of the fluorescence on small changes in the local magnetic field (Figure 1d). In addition,

precise alignment of  $B_0$  along one NV orientation can enable optical polarization of the nitrogen nuclear spin, providing improved ODMR contrast [Fischer *et al.* 2013]. We refer to this approach as projective magnetic microscopy (PMM), because, to a good approximation (supporting information Figure S4), only the component of the sample field projected along the selected NV orientation is detected. As with VMM, each set of PMM measurements consists of magnetic field maps acquired with an aligned and an antialigned bias field relative to the chosen [111] lattice direction. The sum and difference of these two maps yield the magnetic fields due to remanent and induced magnetizations, respectively. PMM can enhance sensitivity by a factor of  $\sim 2$ – $3$  compared with typical VMM, although the largest gains are available only if the range of sample magnetic field values to be imaged,  $\Delta B_{\text{sample}}$ , is small, (i.e.,  $\mu_B \Delta B_{\text{sample}} \ll \Gamma_{\text{NV}}$ , for  $\Gamma_{\text{NV}}$  the NV ODMR half width and at half maximum (HWHM) linewidth defined in supporting information Figure 4), such that the frequency sweep range may be restricted to the sharpest part of the resonance [Glenn *et al.*, 2015]. This tradeoff between sensitivity and dynamic range is generic for NV ODMR measurements. Another potential drawback of PMM is that CVD diamond chips are typically grown with [100] normal to the sensing plane, such that the magnetic projection direction in PMM measurements is at an angle of  $54.7^\circ$  to the normal. Diamond chips with [111] normal to the plane can be produced by cleaving or polishing at the appropriate angle, usually at the expense of a smaller available field of view.

### 2.2.3. Circularly Polarized Magnetic Microscopy (CPMM)

Bias fields  $B_0 \geq 1$  mT are necessary during data acquisition in the VMM and PMM configurations to spectrally resolve the projected field magnitude along different NV orientations. Although the sum of successive measurements under a reversed  $B_0$  rejects the induced magnetic response of the sample to  $B_0$  during a measurement, down to the residual bias  $B_0^{(r)} < 0.1$   $\mu\text{T}$ , inaccuracy in the reversal of the bias field may introduce systematic errors. To avoid this potential problem and recover only the magnetic fields due to remanent magnetization without exposing the sample to significant magnetic fields, we adapt a single-axis ODMR technique (Figure 1e) previously demonstrated [Alegre *et al.*, 2007] to work at very small bias ( $B_0 < 10$   $\mu\text{T}$  in our system), by using a drive field  $B_1$  that is circularly polarized with respect to  $B_0$ .

The  $B_0$  field is aligned normal to the diamond surface such that it projects equally on all NV orientations. In this configuration, the component of the sample magnetic field parallel to  $B_0$  produces asymmetric shifts of the four sets of degenerate ODMR resonances relative to the zero-field splitting frequency, with the sign of the shift depending on the handedness of  $B_1$ . By switching between left-circular and right-circular drive fields, the centroid of the degenerate resonance lines is modulated to higher or lower frequency, allowing detection of small shifts,  $g \mu_B B \ll \Gamma_{\text{NV}}$ . The data shown in Figure 1e were obtained at  $B_0 = 40$   $\mu\text{T}$ , where the  $\Delta m_s = +1$  and  $\Delta m_s = -1$  transitions are resolved, to clearly illustrate the procedure. However, small line shifts can be detected even in the unresolved case, in practice. Sample magnetic fields perpendicular to  $B_0$  give rise instead to a symmetric broadening of the degenerate resonances, and therefore cannot easily be detected. We refer to this approach as circularly polarized magnetic microscopy (CPMM). CPMM is typically performed with NV centers formed from  $^{15}\text{N}$ , which have simpler spectra than NV centers formed from  $^{14}\text{N}$  (i.e., hyperfine doublets instead of triplets). Despite the extra technical overhead of the circularly polarized NV drive, as well the need for careful calibration when strain terms in the NV Hamiltonian become comparable to the Zeeman term (see section 3.3), this is the only technique known to us that enables NV magnetic imaging at very low bias field. (See supporting information Figure S5 for an extended discussion of the CPMM technique.)

## 3. Measurements and Discussion

The high spatial resolution of the QDM, together with the ability to acquire optical and magnetic images simultaneously, enables local magnetic field maps to be precisely correlated with images of petrographic structure obtained in other instruments. To illustrate the constraints on ferromagnetic mineralogy offered by these measurements, we acquired coregistered optical and magnetic maps of three different rock samples, each of which displays heterogeneous magnetization at the 1–100  $\mu\text{m}$  scale.

### 3.1. Correlative Optical and Magnetic Microscopy

As an example QDM application, we acquired spatially correlated optical magnetic images of a 30  $\mu\text{m}$  thin section of the Allende CV3 chondrite to identify the primary or secondary origin of ferromagnetic carriers. As in the case of most chondrites, Allende contains millimeter scale igneous chondrules embedded in a

finer-grain matrix consisting of primitive and recrystallized minerals. Early paleomagnetic studies have suggested that Allende chondrules recorded primordial solar system magnetic fields as they formed and cooled in the solar nebula [Lanoix *et al.*, 1978; Sugiura and Strangway, 1985]. However, subsequent paleomagnetic studies of Allende have revealed pervasive recrystallization of ferromagnetic phases, including the formation of pyrrhotite, magnetite, and awaruite during metasomatism on the CV parent body [Carpurzen *et al.*, 2011; Fu *et al.*, 2014b]. The identification of ferromagnetic phases within individual chondrules is therefore necessary to assess the interpretation of chondrule remanent magnetization due to nebular magnetic fields. If the ferromagnetic mineralogy of chondrules consists of secondary minerals, the chondrules cannot preserve magnetization acquired prior to the accretion of the parent body.

To facilitate the identification of magnetic sources inside individual chondrules, we imparted a strong in-plane isothermal remanent magnetization (IRM) in a 200 mT field on a 30  $\mu\text{m}$  thick section of Allende. Although this applied field does not saturate the pyrrhotite grains present in Allende, it covers the majority of the coercivity range within which the NRM is observed [Carpurzen *et al.*, 2011]. We therefore regard our maps of the 200 mT IRM as a satisfactory approximation of the distribution of ferromagnetic grains carrying NRM in the Allende meteorite. The diamond D1 (with  $^{14}\text{NV}$  layer depth of  $\sim 20$  nm—see supporting information Table S1) was placed directly onto the sample, such that the effective standoff distance to the sensor was set by the roughness of the polished sample surface ( $\sim 1\text{--}3$   $\mu\text{m}$ , estimated by high-magnification optical microscopy). The full field of view (FOV) had dimensions  $\sim 800$   $\mu\text{m} \times 600$   $\mu\text{m}$ . Comparison of the reflected light, plane-polarized image (Figure 2a), and VMM magnetic map (Figure 2b, acquired in  $1.5 \times 10^3$  s of averaging) shows the concentration of ferromagnetic carriers in the rim and mesostasis regions of the chondrule. Reflected-light microscopy indicates that the chondrule rim contains abundant magnetite. Meanwhile, although the ferromagnetic phases in the mesostasis regions of our measured chondrule were not visible in optical microscopy, previous analyses have shown that they also contain exclusively mineral assemblages formed during aqueous alteration [Brearley and Krot, 2012]. As such, the spatial localization of ferromagnetism in these areas using the QDM indicates the secondary nature of ferromagnetic grains from Allende chondrules [Fu *et al.*, 2014b].

A similar application of the QDM to image a strong artificial magnetization has already been demonstrated in the literature [Fu *et al.*, 2014a], as a means to identify the mineralogy of the strongest sources in the sample *after* the volume-averaged natural remanence had been extracted by conventional thermal or alternating-field demagnetization. In principle, it should be possible to obtain spatially resolved demagnetization curves within each magnetically homogeneous subregion of a QDM image directly, although this technology has yet to be implemented.

To test the repeatability of QDM magnetic field maps, as well as the agreement between different ODMR acquisition modes, we reimaged a smaller field of view (sub-FOV) of the Allende chondrule containing several altered mesostasis regions using diamond D2 (with a  $^{15}\text{NV}$  layer depth of  $\sim 20$  nm) in VMM and CPMM (Figure 2c). The diamond position and laser illumination pattern were kept fixed between the two measurements; only the direction of  $B_0$  and the polarization and frequency sweep range of  $B_1$  were changed. Each image was acquired in  $2.0 \times 10^4$  s of averaging. After mean-subtraction to account for the difference in  $B_0$ , the field maps showed good qualitative agreement, with all of the dipolar magnetic features from the full FOV map clearly discernible in the new sub-FOVs. However, careful comparison shows that the peak field values of magnetic features measured in CPMM are greater than those in VMM, typically by  $\sim 5\text{--}10\%$ . This suggests the need for calibration of the different ODMR imaging techniques, as described in the following sections. In addition, we note that the full FOV field map contains a prominent, sharp noise feature (white arrow) that does not appear in either of the sub-FOVs. We attribute this to local diamond-strain-induced shifts in NV resonance frequencies in the affected pixels, likely due to an edge dislocation in the diamond crystal running perpendicular to the chip surface. (Changing to a different diamond for the sub-FOVs thus eliminated the feature.) Because such crystal defects produce strong strain fields that are not completely accounted for by our NV Hamiltonian fitting procedure, their positions must be recorded for each diamond and the affected pixels excluded from measured magnetic field maps.

### 3.2. Illustration of Sensitivity and Spatial Resolution

To establish performance benchmarks for rock magnetometry with the QDM, we obtained maps of magnetic fields produced by remanent magnetization in a 30  $\mu\text{m}$  thin section from the eucrite ALHA81001

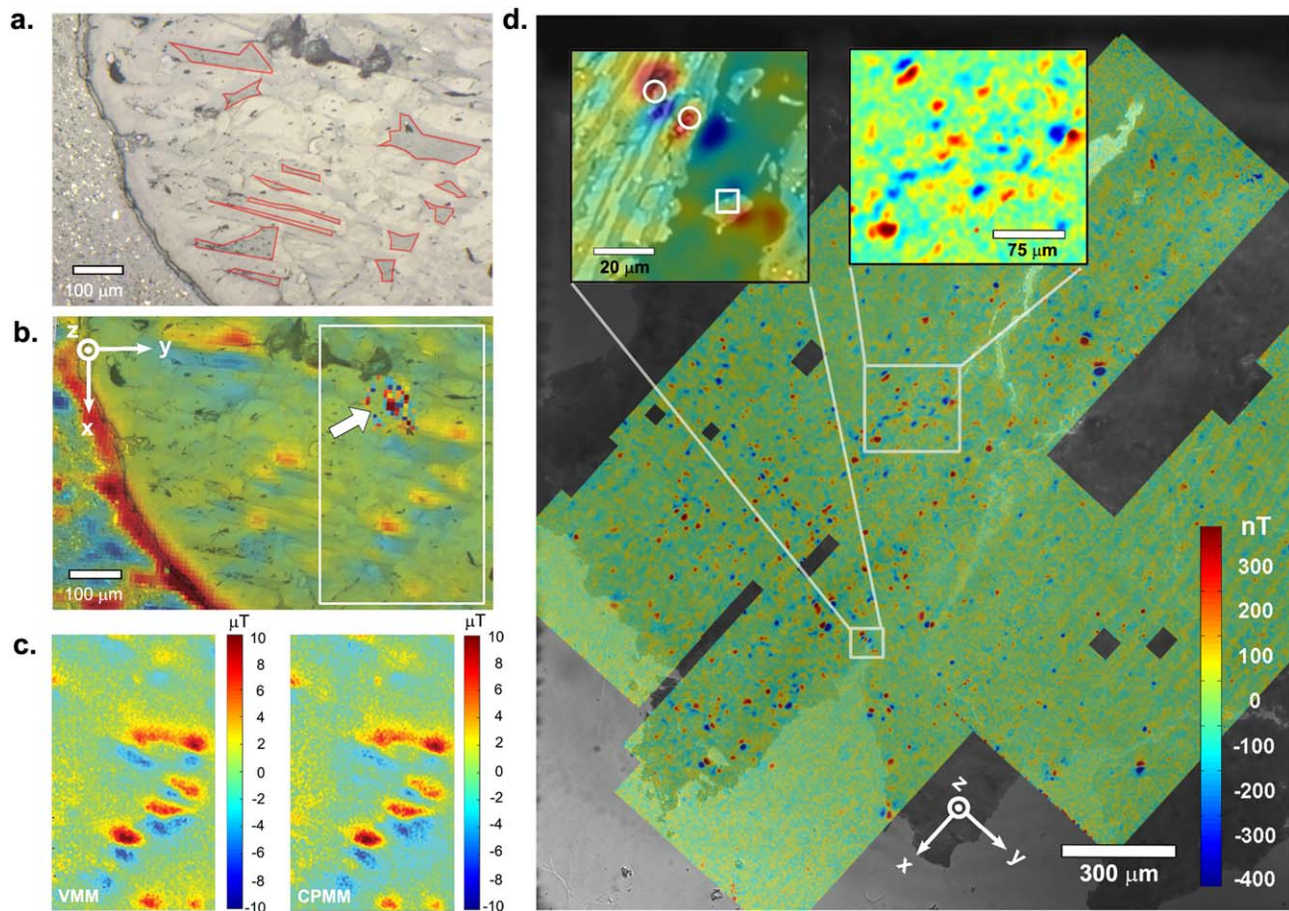


**Figure 2.** QDM magnetic field maps of remanent magnetization and spatially correlated optical images of meteorites. (a) Reflected-light image (plane-polarized illumination) of a 30  $\mu\text{m}$  thin section of a chondrule from the Allende CV3 chondrite. Mesostasis regions are outlined in red. (b) Magnetic map of the  $B_z$  (out-of-plane) component of the field distribution produced by the sample, acquired in VMM and overlaid on the same reflected-light image. White arrow indicates a distortion of the field map due to a localized diamond defect. Such defects are fixed in the diamond volume and may be removed from the FOV by translating the sensor relative to the sample [as in Figure 2c]. (c) Comparison of (left) VMM and (right) CPMM field maps of the subregion of Figure 2b enclosed in the white box. The residual bias after field reversal ( $B_0^{(r)}$ ) has been subtracted from the VMM map; the full bias ( $B_0$ ) has been subtracted from the CPMM map. The resulting magnetic field images are qualitatively similar, but peak recorded field intensities differ by up to  $\sim 10\%$ , illustrating the need for independent calibration of CPMM. (d) Overlay of a  $B_z$  (out-of-plane) VMM magnetic field map and reflected light photomicrograph of a 30  $\mu\text{m}$  thin section from the weakly magnetized eucrite ALHA81001. The magnetic map is composed of four tiled and partially overlapping FOVs, with several small regions removed due to known strain defects in the diamond. The QDM data have spatial resolution  $\sim 5 \mu\text{m}$  and a noise floor of  $\sim 20 \text{ nT}$  RMS. (inset top left) Backscattered electron (BSE) image of a small region of the sample, overlaid with the QDM-acquired  $B_z$  map of the same region. The magnetic map was used to guide energy dispersive spectroscopy (EDS) analysis at select locations with strong magnetic sources, which found elemental abundances associated with chromite (white circles) and metallic iron (white square). (inset top center) Zoomed-in region of the QDM magnetic field image (with limits indicated by solid white box), demonstrating the spatial resolution of the instrument.

(Figure 2d; full vector dataset in supporting information Figure S6). Large-scale metal-silicate differentiation on the eucrite parent body, likely the asteroid Vesta, led to the generation of a core dynamo and remanent magnetization like that recorded by ALHA81001 [Fu *et al.*, 2012]. ALHA81001 and other eucrites exhibit very weak remanent magnetization due to the low abundance of metal grains [Rochette *et al.*, 2003], making ALHA81001 a stringent test for QDM sensitivity. At the same time, the QDM can aid in the identification of the main ferromagnetic carrier phases in ALHA81001. Based on probable observed Curie temperatures at 320–350°C and  $>700^\circ\text{C}$ , Fe sulfide and Fe metal have been identified as the most likely remanence carriers [Fu *et al.*, 2012]. However, scanning electron microscopy only located Fe sulfides with the composition of troilite, which is paramagnetic at room temperature, and did not isolate grains of Fe metal with high certainty.

Similar to the experiments on Allende, we placed diamond D1 directly on the surface of the ALHA81001 thin section. (In this case, however, no IRM was imparted to the sample prior to measurement.) Magnetic fields due to remanent magnetization were imaged by VMM in a series of partially overlapping FOVs, each with area 1.5 mm  $\times$  0.6 mm, with bias  $B_0 = 1.44 \text{ mT}$  oriented along unit vector  $(0.17 \hat{x} + 0.94 \hat{y} + 0.30 \hat{z})$  in

the sensor coordinate system. We used a total averaging time of  $\sim 4 \times 10^4$  s for each FOV, with an optical excitation intensity  $\sim 10^6$  W/m<sup>2</sup> and imaging pixel size of  $(2.4 \mu\text{m})^2$ . Spatial filters were applied in postprocessing, including a 5  $\mu\text{m}$  FWHM Gaussian low-pass to improve the signal-to-noise ratio (SNR), and a 200  $\mu\text{m}$  Butterworth high-pass to eliminate offsets in each FOV associated with our nonzero residual bias  $B_0^{(r)}$ . After this procedure, we obtained a magnetic noise floor of  $\sim 20$  nT RMS, estimated by calculating the pixel-wise magnetic field standard deviation for image regions where no sources were present. The sharpest magnetic features observed were on length scales of 5–10  $\mu\text{m}$  and were not blurred significantly by filtering (Figure 2d, top center inset). To distinguish between features produced by sources within the sample and those due to strain features or magnetic contaminants on the diamond surface, we rotated the diamond 90° and repeated the measurement for each FOV (supporting information Figure S7). Spurious strain-induced patterns were manually removed from the image, resulting in several blank areas in the map shown in the figure. These could be filled in by translating or rotating the diamond and measuring again, but were retained here for illustrative purposes. The measurement noise floor corresponds to an image-area-normalized magnetic field sensitivity of  $\sim 20 \mu\text{T} \cdot \mu\text{m}/\text{Hz}^{1/2}$  at long averaging times over a  $\sim 1 \text{ mm}^2$  FOV, which is typical VMM performance for the present QDM for diamonds D1 and D2 with NV layer thickness  $t_{\text{NV}} \approx 10$  nm (supporting information Figure S8).

Guided by the high-resolution QDM magnetic maps, we identified three strongly magnetized locations in ALHA81001 (Figure 2d, top left inset) for compositional analysis using energy dispersive spectroscopy (EDS). These measurements were performed on a Zeiss EVO 60 environmental scanning electron microscope (ESEM) at the American Museum of Natural History (AMNH). Although the  $\leq 1 \mu\text{m}$  diameters of the grains of interest precluded quantitative measurements of composition, we found that magnetization is spatially associated with (i) an Fe-bearing phase with no other transition metals or sulfur, interpreted to be Fe metal, and (ii) an Fe-Ni-Cr-bearing phase, interpreted to be nonstoichiometric chromite (supporting information Figure S9). The identification of Fe metal is consistent with the  $>700^\circ\text{C}$  Curie temperature observed during thermal demagnetization [Fu *et al.*, 2012]. Meanwhile, chromite in terrestrial rocks have been observed to demagnetize between 300°C and 400°C [Kumar *et al.*, 1984], again consistent with the demagnetization behavior of ALHA81001. If this interpretation is correct, ALHA81001 would be the second achondrite after the martian orthopyroxenite ALH84001 where spatial correlation of magnetic field sources suggests chromite as a ferromagnetic carrier [Weiss *et al.*, 2002]. Because our EDS characterization of the Fe-Ni-Cr-bearing phase lacks the spatial resolution necessary to quantify the composition, we cannot make a positive identification of chromite or rule out the possibility of unresolved, nanoscale intergrowths of, for example, Fe metal that carry the observed magnetization. Future TEM-based work is required to address these ambiguities. Even so, a Fe-Ni-Cr-bearing phase likely crystallized during the primary cooling of ALHA81001 on its parent body, as it is not consistent with terrestrial weathering products [Buchwald and Clark, 1989]. As such, our QDM measurements provide further support for the extraterrestrial origin of magnetization on ALHA81001.

The QDM magnetic sensitivity demonstrated in our map of the ALHA81001 thin section can likely be improved for many applications by increasing the NV layer thickness,  $t_{\text{NV}}$ . The transverse spatial resolution of the QDM is generally limited by the sensor-sample standoff distance  $d_{s-s}$ , and the NV layer thickness can be increased up to a significant fraction of  $d_{s-s}$  without adversely affecting the resolution (supporting information Figure S10). Proposed QDM paleomagnetic imaging applications require spatial resolution of  $\sim 1$ –100  $\mu\text{m}$  to resolve ferromagnetic grain populations in a wide range of geological samples, suggesting that the thin NV layers of D1 and D2 (with  $t_{\text{NV}} \approx 10$  nm) should be replaced with thicker NV layers to enable more sensitive detection. For example, a diamond with NV layer thickness  $t_{\text{NV}} = 10 \mu\text{m}$  and equal NV density to a diamond with  $t_{\text{NV}} \approx 10$  nm will produce  $\sim 10^3$  times higher fluorescence at the same illumination intensity, yielding an SNR improvement of  $\sim 30$  for photon shot-noise limited detection. Thick NV layer diamonds can be produced by doping with high N concentration during the last stage of CVD growth, followed by electron irradiation and annealing to create NV centers. To date, we have tested one such thick-NV-layer diamond, D3, and applied it successfully to large-FOV magnetic imaging studies of zircons (see discussion in section 3.4). We have yet to optimize the QDM for the high-throughput fluorescence collection needed to obtain maximum SNR improvement from thick-NV-layer diamonds when using smaller FOVs.

To achieve optimal spatial resolution and sensitivity in future QDM imaging applications, geological sample thickness,  $t_{\text{sample}}$ , will also be an important consideration. Because inversion of magnetic field maps to obtain volume distributions of dipolar sources in the sample is in general an ill-posed problem, the highest

confidence determination of magnetization distribution uses samples with large area relative to their thickness [Lima et al., 2013]. This requirement imposes a practical bound on QDM standoff distance and hence the imaging resolution,  $d_{s-s} \gg t_{\text{samp}}$ . The sample thickness constraint is relevant to the ALHA81001 field

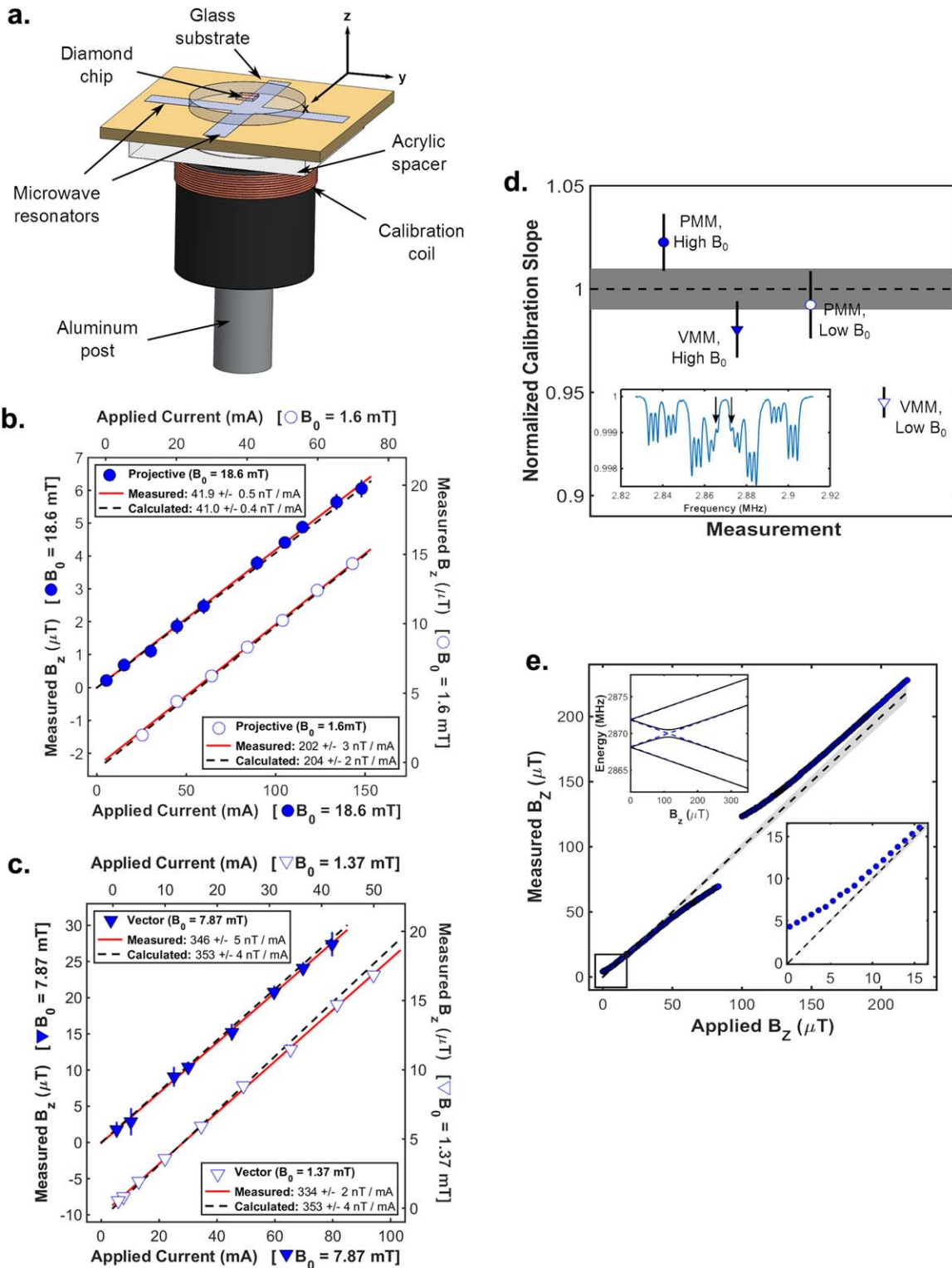


Figure 3. (continued)

maps, where the QDM is most sensitive to sources in the top 5  $\mu\text{m}$ . For the chosen QDM resolution, a much thinner rock section would be preferable for unambiguous determination of sample magnetization.

### 3.3. Accuracy of Magnetic Field Measurements

Absolute accuracy of magnetic field maps is necessary for correct determination of sample remanence and for proper comparison of magnetic measurements made in different devices. When ODMR spectra are acquired for both the  $\Delta m_s = +1$  and  $\Delta m_s = -1$  transitions, the accuracy of the QDM is relatively insensitive to temperature variations and other systematic effects that result in equal frequency shifts for the two resonances. Nevertheless, the linearity of magnetic field-induced spectral line shifts may break down at small  $B_0$ , when the Zeeman term in the NV Hamiltonian becomes comparable to nuclear hyperfine couplings and strain [Doherty *et al.*, 2013; Barson *et al.*, 2017; Felton *et al.*, 2009]. We therefore calibrated the QDM by incorporating an additional coil under the sample holder so as to produce uniform, well-defined fields perpendicular to the sensor surface (Figure 3a). Coil currents were driven using a diode laser driver and the coil geometry was precisely measured in an optical microscope, such that the expected magnetic field could be calculated with uncertainty  $<1\%$  (supporting information Figure S11). We first obtained calibration curves of measured  $B_z$  as a function of applied current for PMM (Figure 3b) and VMM (Figure 3c) using diamond D4 at both high and low bias fields ( $B_0 = 18.6$  mT and  $B_0 = 1.6$  mT, respectively). The measured slope agreed well with calculations (Figure 3d) to within the estimated uncertainty (grey band is  $1\sigma$  in figure), except in the case of VMM at low  $B_0$ . This deviation was likely due to strain inhomogeneity over the imaged region, which can cause line shifts as large as  $\sim 1$  MHz in D4. The NV orientation with the smallest projection of  $B_0$  may experience a Zeeman shift of only a few MHz in low-bias VMM, such that strain significantly broadens and/or shifts the spin transition frequencies for this orientation (Figure 3d, inset). This is an important potential drawback of VMM at low  $B_0$ .

Diamond strain and NV hyperfine effects may play an even greater role for CPMM imaging at low bias,  $B_0 < 0.2$  mT. In this mode, we use only diamonds with NVs formed from  $^{15}\text{N}$  (nuclear spin  $I = 1/2$ ) implants, to avoid the spectral congestion and inhomogeneity associated with transitions involving  $m_l = 0$  states (for which the absence of hyperfine coupling makes strain the dominant interaction) in NVs formed from  $^{14}\text{N}$  ( $I = 1$ ). Nevertheless, sensor calibration is still essential to extract accurate magnetic field values, as demonstrated in our measurements on diamond D2 (Figure 3e). We observed a strong deviation from linearity in the QDM response for  $B_z \approx 112$   $\mu\text{T}$ , where the Zeeman and hyperfine energies are approximately equal, due to a transverse-strain-induced anticrossing between energies of the  $|m_s = \pm 1, m_l = \mp 1\rangle$  states. In addition, our spectral fitting algorithm was unable to determine independent line shape parameters for the transitions near degeneracy, resulting in a gap in our calibration. A second deviation from linearity for  $B_z < 20$   $\mu\text{T}$  (Figure 3e, bottom inset) could also be attributed to strain. Because these nonlinearities are due to fixed material properties of the diamond chip, the calibration is repeatable (for a given FOV) and exact to within the accuracy of the applied calibration field.

### 3.4. Reconfigurable Multiscale Imaging for Magnetic Surveys

The magnetic signal-to-noise ratio (SNR) of the QDM varies inversely with the laser excitation spot diameter in the shot-noise detection limit, for fixed laser power. It is therefore technically straightforward to alternate between rapid, wide-FOV magnetic mapping and targeted, sensitive acquisition in a small region of interest,

**Figure 3.** Absolute magnetic field calibration of the QDM. (a) QDM calibration setup schematic. A precisely characterized coil, placed below the diamond chip, generated known magnetic fields at the NV sensing layer. The ODMR signal was averaged over a  $1.0$  mm  $\times$   $0.5$  mm FOV, and the resulting measured magnetic fields compared against the calculated coil field. (b) Magnetic field values obtained in PMM as a function of coil current, for both high bias ( $B_0 = 18.6$  mT, closed circles) and low bias ( $B_0 = 1.6$  mT, open circles). Linear fits to the data (red lines) are consistent with the calculated fields (black dashed lines) for each current value. (c) Magnetic field values obtained in VMM as a function of coil current, for both high bias ( $B_0 = 7.87$  mT, closed triangles) and low bias ( $B_0 = 1.37$  mT, open triangles). A linear fit to the data (red lines) is consistent with the calculated fields (black dashed lines) for the high bias case, but differs by more than the estimated uncertainty in the calculation for the low bias case. (d) Summary of fit slopes from Figures 3b and 3c, normalized to the calculated value. Grey band indicates uncertainty ( $1\sigma$ ) in the calculated slope. Error bars on the individual measured slopes are also  $1\sigma$ . (inset) Characteristic low- $B_0$  VMM spectrum, with the innermost peaks (black arrows) broadened by transverse strain. (e) CPMM calibration, showing measured magnetic field versus expected field as calculated from the applied current. Black dashed line is the ideal calibration with unit slope; grey band indicates uncertainty in the calculation. Measurements (blue data points) differ significantly from the ideal curve due to a transverse strain-induced avoided crossing. (inset bottom right) Zoomed-in data for  $B_z < 10$   $\mu\text{T}$ . The measured magnetic field is nonzero at zero applied field due to a finite splitting induced by transverse strain. (inset top left) Calculated energy structure of the  $m_s \neq 0$  NV spin states as a function of applied magnetic field for a nominal transverse strain parameter of  $0.5$  MHz (black curve), compared to the zero-strain case (dashed blue curve). Strain results in an avoided crossing, as well as a small additional splitting of the energies at zero magnetic field.

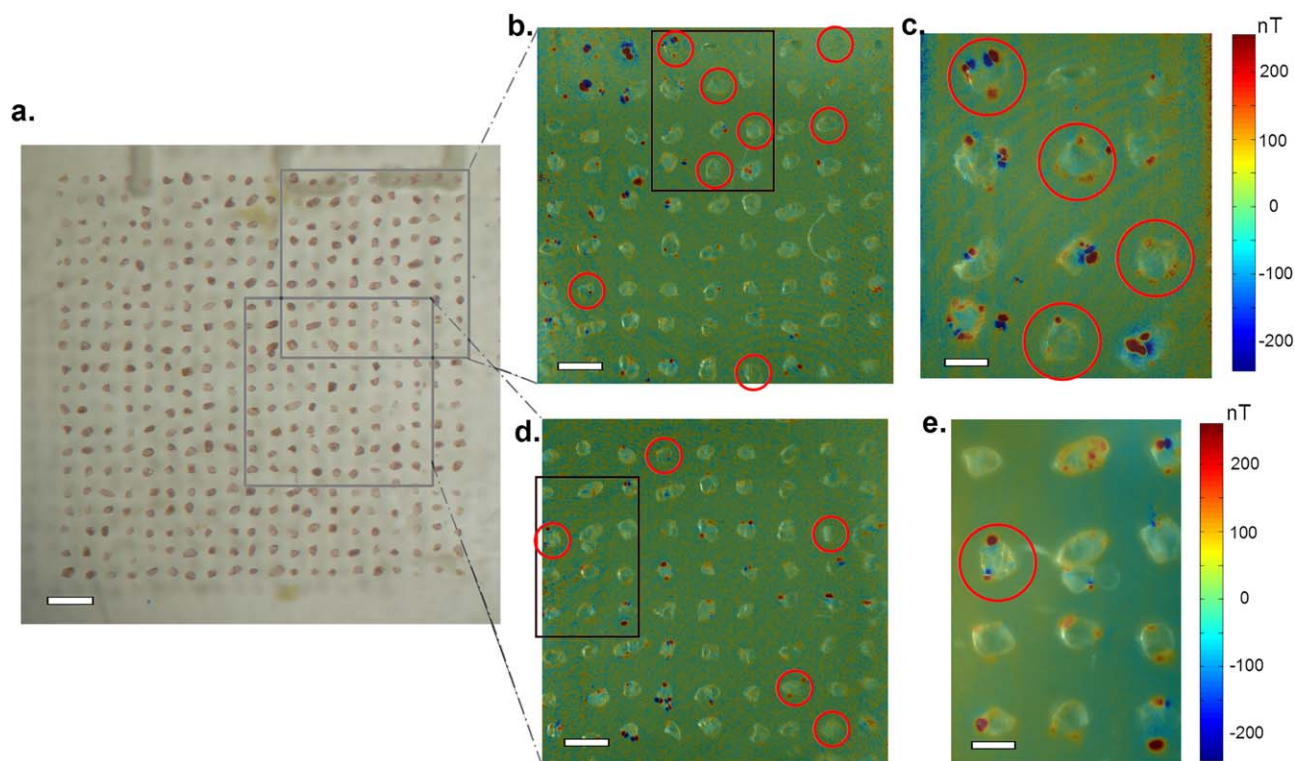


**Figure 4.** Multiscale QDM survey of magnetic sources in Jack Hills zircons. (a) Reflected-light image of a matrix of zircons from the Jack Hills of Western Australia, embedded in epoxy. Grey boxes show two characteristic FOVs for which VMM magnetic field maps were obtained. Scale bar is 1 mm. (b) Reflected-light image of upper FOV, with the  $B_z$  (out-of-plane) component of the VMM magnetic map overlaid. The magnetic data acquisition was optimized to allow rapid imaging of a large ( $\sim 13 \text{ mm}^2$ ) field of view. Red circles indicate zircons  $>3.9 \text{ Ga}$  in age. Scale bar is  $500 \mu\text{m}$ . Color scale (not shown) is  $-500$ – $500 \text{ nT}$ . (c) Reflected-light image of zoomed-in region in upper FOV, with the  $B_z$  (out-of-plane) component of the VMM magnetic map overlaid. The magnetic data acquisition was optimized for magnetic field sensitivity and spatial resolution. Magnetic features qualitatively agree with those observed in Figure 4b, although more features are visible due to the improved sensitivity. Scale bar is  $200 \mu\text{m}$ . Color scale is  $-250$ – $250 \text{ nT}$ . (d) Reflected-light image of lower FOV, with the  $B_z$  (out-of-plane) component of the VMM magnetic map overlaid. Red circles indicate zircons  $>3.9 \text{ Ga}$  in age. Scale bar is  $500 \mu\text{m}$ . Color scale (not shown) is  $-500$ – $500 \text{ nT}$ . (e) Reflected-light image of zoomed-in region of lower FOV, with the  $B_z$  (out-of-plane) component of the VMM magnetic map overlaid. Scale bar is  $200 \mu\text{m}$ . Color scale is  $-250$ – $250 \text{ nT}$ .

simply by changing lenses in the optical excitation and fluorescence collection paths. This capability is advantageous in applications where a large sample area must be quickly screened to find magnetic features of interest. To demonstrate, we surveyed a group of detrital zircons from the Jack Hills region in Western Australia (Figure 4). The Jack Hills zircons are the oldest known samples of the Earth's crust, with ages ranging up to 4.38 billion years [Holden *et al.*, 2009]. As such, their magnetizations may potentially contain the earliest paleointensity records of the geodynamo [Tarduno *et al.*, 2015]. However, the presence of multiple metamorphic and metasomatic events in the locality suggests that their ferromagnetic phases may not be primary, but deposited in cracks and on the zircon exterior well after the formation of the zircon [Weiss *et al.*, 2015, 2016]. This possibility can be assessed by resolved magnetic imaging of zircons to determine the spatial distribution of their magnetization.

With this goal, we imaged the magnetization of 257 zircons using the QDM. The zircons were extracted from the host quartz-pebble conglomerate using a Frantz Model LB-1 Magnetic Separator at Australia National University (in which the grains were exposed to fields up to 1.6 T), washed in alcohol and then mounted in an epoxy disk and polished to approximately their midsections. They were then dated with Pb-Pb chronometry using secondary ion mass spectrometry at UCLA following the methods of Holden *et al.* [2009]. Following this this, they were given an isothermal remanent magnetization (IRM) in a field of 140 mT, oriented perpendicular to the plane of the epoxy disk and then measured with VMM. (Also see the supporting information of Fu *et al.* [2017] for the discussion of a similar QDM imaging procedure applied to zircons from the Bishop Tuff.) Our analyzed samples included 22 grains with Pb-Pb ages greater than 3.9 Ga.

We first acquired coarse VMM magnetic maps of a subset ( $n = 257$ ) of the zircons over four large FOVs ( $3.6 \text{ mm} \times 3.6 \text{ mm}$ ) with diamond D3, using an achromatic doublet lens (focal length  $F = 5 \text{ cm}$ , numerical aperture  $NA = 0.25$ ) for fluorescence collection. The tube lens for all zircon-imaging experiments was also

an achromatic doublet,  $F = 15$  cm. Each FOV was acquired using pixel size  $(8.7 \mu\text{m})^2$  and averaging time  $1.8 \times 10^4$  s, yielding a noise floor of  $\sim 70$  nT RMS. (Two of these FOVs are indicated in Figure 4a.) At this resolution, 147 out of 257 of zircons mapped produced magnetic signals distinguishable from background, although 122 of these were due to sources distributed on the exterior surface of the zircon. To assign magnetic features, coregistered magnetic and reflected-light images were overlaid and inspected visually (Figures 4b and 4d). Magnetic sources were defined to be on the exterior of a zircon if the center of the dipole field pattern fell within  $\sim 20 \mu\text{m}$  of the boundary of that zircon in the reflected-light image. The mix of magnetization directions observed from the zircon ferromagnetic sources is due to the combined effects of strong fields during magnetic separation and a weaker, 140 mT IRM in the out-of-plane direction.

We then changed to a higher magnification aspherized achromat lens ( $F = 1.4$  cm,  $NA = 0.45$ ) for light collection, and focused the excitation laser spot down to an area of  $1.6 \text{ mm} \times 1.2 \text{ mm}$ . This allowed us to zoom in on smaller FOVs that contained a high fraction of zircons dated to  $>3.9$  Ga. We acquired maps of six such FOVs using a pixel size of  $(3.6 \mu\text{m})^2$  and averaging time of  $1.8 \times 10^4$  s, resulting in a noise floor of  $\sim 25$  nT RMS. Field maps at the higher resolution were consistent with those of the original four large FOVs, but more magnetic features were visible due to the improved sensitivity and spatial resolution (Figures 4c and 4e). Of the 78 zircons measured under these conditions, 71 now had detectable magnetic signatures, with 52 of those clearly attributable to sources on the exterior of the zircon. These results contrast with our QDM study of young (767 ka) relatively unaltered zircons from the Bishop Tuff [Fu *et al.*, 2017], which found that most of the magnetization is in the interior of the grains. Therefore, the present results emphasize that the natural remanent magnetization (NRM) in Jack Hills zircons [Tarduno *et al.*, 2015] could be far younger than their crystallization ages. In particular, because Tarduno [2015] measured the bulk NRM of zircons rather than imaging the NRM distribution, their data do not constrain where in the grains the magnetization carriers reside. A caveat is that these QDM data are images of IRM rather than NRM. In any case, these results also illustrate the flexibility of the QDM for imaging at different scales, from coarse surveys of large ( $\sim 10$ – $20 \text{ mm}^2$ ) FOVs, to detailed maps of smaller FOVs ( $\sim 1 \text{ mm}^2$ ) with improved sensitivity, and hence better fidelity in detection of weak magnetic sources.

#### 4. Conclusion

We constructed a new instrument, the quantum diamond microscope (QDM), for imaging magnetic fields from room-temperature geological samples with spatial resolution  $\sim 5 \mu\text{m}$ . The QDM also provides optical images of the sample that are spatially correlated with the magnetic images. The device can be operated in three modes, including (i) a vector (three-axis) magnetic imaging mode, (ii) a projective (single-axis) mode optimized to improve magnetic field sensitivity by a factor of 2–3, and (iii) a single-axis mode using circularly polarized microwaves that allows operation at low bias  $B_0 < 10 \mu\text{T}$ . The first two modes (VMM and PMM) provide superior absolute accuracy in magnetic field estimation ( $\sim 1\%$  without calibration), particularly at  $B_0 > 10 \text{ mT}$ , but rely on precise bias reversal (with  $B_0^{(r)} < 0.1 \mu\text{T}$ ) to distinguish between paramagnetic and ferromagnetic sources. The third mode (CPMM) avoids the bias-reversal constraint by operating at low ambient field, but requires careful calibration to account for strain-induced shifts in the NV ODMR spectra. The typical image-area-normalized magnetic field sensitivity of the present QDM is  $\sim 20 \mu\text{T} \cdot \mu\text{m} / \text{Hz}^{1/2}$  for a  $1 \text{ mm} \times 1 \text{ mm}$  FOV, and scales linearly with the diameter of the FOV for fixed laser power. The best demonstrated noise floor is  $\sim 20$  nT RMS. We recently began to work with diamond chips that possess considerably thicker NV layers than were previously available ( $\sim 10 \mu\text{m}$  rather than  $\sim 10 \text{ nm}$ ), which are expected to provide a sensitivity improvement of  $\sim 30\times$  with the implementation of a faster camera and data acquisition system. We used the QDM to image magnetic fields from a variety of magnetically heterogeneous rock samples, and confirmed that we can distinguish populations of ferromagnetic carriers separated by  $< 10 \mu\text{m}$ . In particular, QDM imaging shows that magnetization carriers in ancient zircon crystals from the Jack Hills of Western Australia are largely confined to the exteriors of most grains, suggesting that their ferromagnetic minerals are secondary in origin and therefore that they do not retain pristine records of the earliest history of the dynamo.

A number of technical improvements are planned for future QDM systems, including (i) tools for rapid sample exchange and alignment, to increase measurement throughput and facilitate QDM imaging interspersed with multiple rounds of AF or thermal demagnetization, (ii) improved heatsinking and thermal

stabilization, enabling the use of higher laser power for better QDM sensitivity, and (iii) development of micron-scale magnetic standard samples, to allow quantitative comparison between QDM magnetic maps and those obtained in other instruments at different standoff distances.

### Acknowledgments

We thank the NASA Emerging Worlds and NASA Planetary Major Equipment programs (grant NNX15AH72G), the NSF Integrated Support Promoting Interdisciplinary Research and Education (INSPIRE) program (grant EAR 1647504), the NSF Electronics, Photonics and Magnetic Devices (EPMD) program (grant 1408075), and the DARPA Quantum Assisted Sensing And Readout (QuASAR) program (contract HR0011-11-C-0073) for support. P.K. acknowledges support from the IC Postdoctoral Research Fellowship Program. B.P.W., E.A.L., and R.R.F. thank Thomas F. Peterson Jr. for a generous gift. We also thank T.M. Harrison for providing the Jack Hills zircons used for QDM imaging. Data presented in this work are included in a zip archive in supporting information section S12. Magnetic field and reflected-light images acquired in the QDM are provided in .csv format; high resolution reflected-light images acquired in other instruments are provided as .tif images.

### References

- Acosta, V. M., A. Jarmola, E. Bauch, and D. Budker (2010), Optical properties of the nitrogen-vacancy singlet levels in diamond, *Phys. Rev. B*, *82*, 201,202, doi:10.1103/PhysRevB.82.201202.
- Alegre, T. P. M., C. Santori, G. Medeiros-Ribeiro, and R. G. Beausoleil (2007), Polarization-selective excitation of nitrogen vacancy centers in diamond, *Phys. Rev. B*, *76*, 165,205, doi:10.1103/PhysRevB.76.165205.
- Barson, M. S. J., et al. (2017), Nanomechanical sensing using spins in diamond, *Nano Lett.*, *17*, 1496–1503, doi:10.1021/acs.nanolett.6b04544.
- Brearley, A. J., and A. Krot (2012), Metasomatism in the early solar system: The record from chondritic meteorites, in *Metasomatism and the Chemical Transformation of Rock, Lecture Notes in Earth System Sciences*, edited by D. E. Harlow and H. Austrheim, pp. 659–789, Springer, Berlin, Heidelberg, doi:10.1007/978-3-642-28394-9\_15.
- Buchwald, V. F., and R. S. Clark (1989), Corrosion of Fe-Ni alloys by Cl-containing akaganeite (beta-FeOOH): The Antarctic meteorite case, *Am. Mineral.*, *74*, 656–667.
- Carporzen, L., B. P. Weiss, L. Elkins-Tanton, D. L. Shuster, D. S. Ebel, and J. Gattacceca (2011), Magnetic evidence for a partially differentiated carbonaceous chondrite parent body, *Proc. Natl. Acad. Sci. U.S.A.*, *108*, 6386–6389, doi:10.1073/pnas.1017165108.
- Doherty, M. W., N. B. Manson, P. Delaney, F. Jelezko, J. Wrachtrup, and L. C. L. Hollenberg (2013), The nitrogen-vacancy center in diamond, *Phys. Rep.*, *528*, 1–45, doi:10.1016/j.physrep.2013.02.001.
- Felton, S., A. M. Edmonds, M. E. Newton, P. M. Martineau, D. Fisher, D. J. Twitchen, and J. M. Baker (2009), Hyperfine interaction in the ground state of the negatively charged nitrogen vacancy center in diamond, *Phys. Rev. B*, *79*, 075203, doi:10.1103/PhysRevB.79.075203.
- Fischer, R., A. Jarmola, P. Kehayias, and D. Budker (2013), Optical polarization of nuclear ensembles in diamond, *Phys. Rev. B*, *87*, 125,207, doi:10.1103/PhysRevB.87.125207.
- Fu, R. R., B. P. Weiss, D. L. Shuster, J. Gattacceca, T. L. Grove, C. Sauvet, E. A. Lima, L. Li, and A. T. Kuan (2012), An ancient core dynamo in asteroid vesta, *Science*, *338*, 238–241, doi:10.1126/science.1225648.
- Fu, R. R., et al. (2014a), Solar nebula magnetic fields recorded in the Semarkona meteorite, *Science*, *346*, 1089–1092, doi:10.1126/science.1258022.
- Fu, R. R., E. A. Lima, and B. P. Weiss (2014b), No nebular magnetization in the Allende CV carbonaceous chondrite, *Earth Planet. Sci. Lett.*, *404*, 54–56, doi:10.1016/j.epsl.2014.07.014.
- Fu, R. R., et al. (2017), Evaluating the paleomagnetic potential of single zircon crystals using the Bishop Tuff, *Earth Planet. Sci. Lett.*, *458*, 1–13, doi:10.1016/j.epsl.2016.09.038.
- Glenn, D.R., K. Lee, H. Park, R. Weissleder, A. Yacoby, M. D. Lukin, H. Lee, R. L. Walsworth, and C. B. Connolly (2015), Single-cell magnetic imaging using a quantum diamond microscope, *Nat. Methods*, *12*, 736–738, doi:10.1038/nmeth.3449.
- Gruber, A., A. Draebenstedt, C. Tietz, L. Fleury, J. Wrachtrup, and C. von Borczyskowski (1997), Scanning confocal optical microscopy and magnetic resonance on single defect centers, *Science*, *276*, 2012–2014, doi:10.1126/science.276.5321.2012.
- Hankard, F., J. Gattacceca, C. Fermon, M. Pannetier-Lecoer, B. Langlais, Y. Quesnel, P. Rochette, and S. A. McEnroe (2009), Magnetic field microscopy of rock samples using a giant magnetoresistance-based scanning magnetometer, *Geochem. Geophys. Geosyst.*, *10*, Q10Y06, doi:10.1029/2009GC002750.
- Holden, P., P. Lanc, T. R. Ireland, T. M. Harrison, J. J. Foster, and Z. Bruce (2009), Mass-spectrometric mining of Hadean zircons by automated SHRIMP multi-collector and single-collector U/Pb zircon age dating: The first 100,000 grains, *Int. J. Mass Spectrom.*, *286*, 53–63, doi:10.1016/j.jms.2009.06.007.
- Kawai, J., H. Oda, F. Fujihira, M. Miyamoto, I. Miyagi, and M. Sato (2016), SQUID microscope with hollow-structured cryostat for magnetic field imaging of room temperature samples, *IEEE Trans. Appl. Supercond.*, *26*, 1600,905, doi:10.1109/TASC.2016.2536751.
- Kent, D. V., X. S. Zeng, W. Y. Zhang, and N. D. Opdyke (1987), Widespread late Mesozoic to Recent remagnetization of Paleozoic and lower Triassic sedimentary rocks from South China, *Tectonophysics*, *139*, 133, doi:10.1016/0040-1951(87)90202-2.
- Kletetschka, G., P. Schnabl, K. Šifnerová, Z. Tasáryova, Š. Manda, and P. Pruner (2013), Magnetic scanning and interpretation of paleomagnetic data from Prague Synform's volcanics, *Stud. Geophys. Geod.*, *57*, 103–117, doi:10.1007/s11200-012-0723-4.
- Kumar, A., and M. S. Bhalla (1984), Source of stable remanence in chromite ores, *Geophys. Res. Lett.*, *11*, 177–180, doi:10.1029/GL011i003p00177.
- Lanoix, M., D. W. Strangway, and G. W. Pearce (1978), The primordial magnetic field preserved in chondrules of the Allende meteorite, *Geophys. Res. Lett.*, *5*, 73–76, doi:10.1029/GL005i001p00073.
- Le Sage, D., K. Arai, D. R. Glenn, S. J. Devience, L. M. Pham, L. Rahn-Lee, M. D. Lukin, A. Yacoby, A. Komeili, and R. L. Walsworth (2013), Optical magnetic imaging of living cells, *Nature*, *496*, 486–489, doi:10.1038/nature12072.
- Lima, E. A., B. P. Weiss, L. Baratchart, D. P. Hardin, and E. B. Saff (2013), Fast inversion of magnetic field maps of unidirectional planar geological magnetization, *J. Geophys. Res.*, *118*, 2723–2752, doi:10.1002/jgrb.50229.
- Lima, E. A., A. C. Bruno, H. R. Carvalho, and B. P. Weiss (2014), Scanning magnetic tunnel junction microscope for high-resolution imaging of remanent magnetization fields, *Meas. Sci. Technol.*, *25*, 105,401, doi:10.1088/0957-0233/25/10/105401.
- Maurer, P. C., et al. (2010), Far-field optical imaging and manipulation of individual spins with nanoscale resolution, *Nat. Phys.*, *6*, 912–918, doi:10.1038/NPHYS1774.
- Nakamura, N., K. Okuno, M. Uehara, T. Ozawa, L. Tatsumi-Petrocholis, and M. Fuller (2010), Coarse-grained magnetites in biotite as a possible stable remanence-carrying phase in Vredefort granites, *Geol. Soc. Am. Spec. Pap.*, *465*, 165–172, doi:10.1130/2010.2465(11).
- Pham, L. M., et al. (2011), Magnetic field imaging with nitrogen-vacancy ensembles, *New J. Phys.*, *13*, 045021, doi:10.1088/1367-2630/13/4/045021.
- Robledo, L., H. Bernien, T. van der Sar, and R. Hanson (2011), Spin dynamics in the optical cycle of single nitrogen-vacancy centres in diamond, *New J. Phys.*, *13*, 025013, doi:10.1088/1367-2630/13/2/025013.
- Rochette, P., L. Sagnotti, M. Bournot-Denise, G. Consolmagno, L. Folco, J. Gattacceca, M. L. Osete, and L. Pesonen (2003), Magnetic classification of stony meteorites: 1. Ordinary chondrites, *Meteorit. Planet. Sci.*, *38*, 1–18, doi:10.1111/j.1945-5100.2003.tb00263.x.
- Rondin, L., J.-P. Tetienne, T. Hingant, J.-F. Roch, P. Maletinsky, and V. Jacques (2014), Magnetometry with nitrogen-vacancy defects in diamond, *Rep. Prog. Phys.*, *77*, 056503, doi:10.1088/0034-4885/77/5/056503.
- Schirhagl, R., K. Chang, M. Lorez, and C. L. Degen (2014), Nitrogen-vacancy centers in diamond: Nanoscale sensors for physics and biology, *Annu. Rev. Phys. Chem.*, *65*, 83–105, doi:10.1146/annurev-physchem-040513-103659.

- Sugiura, N., and D. W. Strangway (1985), NRM directions around a centimetersized dark inclusion in Allende, *J. Geophys. Res.*, *90*, C729–C738.
- Swanson-Hysell, N. L., A. C. Maloof, J. L. Kirschvink, D. A. D. Evans, G. P. Halversong, and M. T. Hurtgen (2012), Constraints on Neoproterozoic paleogeography and Paleozoic orogenesis from paleomagnetic records of the Bitter Springs Formation, Amadeus Basin, central Australia, *Am. J. Sci.*, *312*, 817–884, doi:10.2475/08.2012.01.
- Tarduno, J. A., R. D. Cottrell, W. J. Davis, F. Nimmo, and R. K. Bono (2015), A Hadean to Paleoproterozoic geodynamo recorded by single zircon crystals, *Science*, *349*, 521–524, doi:10.1126/science.aaa9114.
- Tauxe, L. (2010), *Essentials of Paleomagnetism*, Univ. of Calif. Press, Berkeley, Calif.
- Uehara, M., C. J. Van Der Beek, J. Gattacceca, V. A. Skidanov, and Y. Quesnel (2010), Advances in magneto-optical imaging applied to rock magnetism and paleomagnetism, *Geochem. Geophys. Geosyst.*, *11*, Q05Y09, doi:10.1029/2009GC002653.
- Weiss, B. P., H. Vali, F. J. Baudenbacher, J. L. Kirschvink, S. T. Stewart, and D. L. Shuster (2002), Records of an ancient Martian magnetic field in ALH84001, *Earth Planet. Sci. Lett.*, *201*, 449–463, doi:10.1016/S0012-821X(02)00728-8.
- Weiss, B. P., E. A. Lima, L. E. Fong, and F. J. Baudenbacher (2007), Paleomagnetic analysis using SQUID microscopy, *J. Geophys. Res.*, *112*, B09105, doi:10.1029/2007JB004940.
- Weiss, B. P., et al. (2015), Pervasive remagnetization of detrital zircon host rocks in the Jack Hills, Western Australia and implications for records of the early geodynamo, *Earth Planet. Sci. Lett.*, *430*, 115–128, doi:10.1016/j.epsl.2015.07.067.
- Weiss, B. P., A. C. Maloof, T. M. Harrison, N. L. Swanson-Hysell, R. R. Fu, J. L. Kirschvink, E. B. Watson, R. S. Coe, S. M. Tikoo, and J. Ramezani (2016), Reply to Comment on “Pervasive remagnetization of detrital zircon host rocks in the Jack Hills, Western Australia and implications for records of the early geodynamo”, *Earth Planet. Sci. Lett.*, *450*, 409–412, doi:10.1016/j.epsl.2016.06.006.